Conference Paper, Published Version

McGovern, David; Rossetto, Tiziana; Todd, David
Tsunami Scour and Forces at Onshore Structures

Tsunami Scour and Forces at Onshore Structures

D. J. McGovern
London South Bank University, London, UK

T. Rossetto
University College London, London, UK

D. Todd
HR Wallingford, UK

Abstract: Tsunami induced scour at onshore coastal structures can cause exposure of the foundations and lead to failure. This paper presents experimental observations of a 147 s crest-led wave inundation, causing scouring and loading on 0.2 m wide square and 0.4 m wide rectangular onshore structures. At 1:50 Froude scale these equate to a 17.3 min inundation at 10 and 20 m wide structures. Scour development is measured using GoPro cameras situated inside the Perspex structures. The hydrostatic load is calculated from the integration of pressure readings along the front face of the structures, and the hydrodynamic loading is estimated from the approach flow velocity, as measured by a Vectrino II profiler. The results show that the maximum scour depth occurs during the inundation before significant slumping decreases the end scour depth. Both the in-test and final scour depths for the 0.4 m structure are greater, due to the larger blockage causing greater acceleration of the flow around the structure. For both structures, the hydrostatic loading is dominant over hydrodynamic load.

Keywords: Tsunami, Scour, Force, Loading, Onshore Structure

1 Introduction

Tsunami, which are commonly generated by under-sea mega-thrust fault motion or landslides, present a hazard to coastal life and the built environment. Recent significant tsunami include the 2004 Indian Ocean tsunami, which resulted in over two hundred and fifty thousand casualties (Telford et al., 2006) and the 2011 Great Eastern Japan Earthquake and Tsunami, which resulted in over fifteen thousand casualties (Kajitani et al., 2013). Post event field surveys widely observe scour at structures, and it is often inferred as the cause of their failure (for example, EEFIT, 2004, Yeh, 2007, EEFIT, 2011, Mori et al., 2012 and Chock et al., 2013). There is a need to develop further understanding of the mechanism and time development of tsunami-induced scour at onshore coastal structures as such knowledge may improve mitigation and structural resilience to scour and, therefore, to failure. To date, investigations of tsunami induced scour are few, particularly of scalable tsunami length waves. This work presents data from an experimental study of onshore tsunami scour that considers tsunami inundation time-scales appropriate to prototype.

Scour currently only has brief mention in the ASCE (2016) ASCE 7-16 Chapter 6: 'Tsunami Loads and Effects' design standards. Herein, a maximum value of scour at a structure of $d_{sc, max} = 1.2H$ for $H < 3.05$m (where H = water height), and $d_{sc, max} = 3.66$m for $H > 3.05$ m is given. This is based on the limited field observations of Tonkin et al., (2013) of scour at structures in the aftermath of the 2011 Great Eastern Japan Tsunami. The geographically localised nature of retrospective and limited field investigations that may only infer post-tsunami scour depths, extents and volumes render them unable to provide systematic elucidation of the processes and mechanisms of tsunami scour.

Laboratory investigations of tsunami scour are also limited. Tonkin et al., (2003) and Nakamura et al., (2008) both use solitary waves to represent tsunami inundation and scour at onshore circular and square cylinders respectively. Madsen et al., (2008), however, shows that the dependency of period and length of solitary waves leads to unrealistic waveforms when scaled up to prototype. Therefore,

the appropriateness of these investigations is uncertain when applied to full scale tsunami. McGovern et al., (2019) conducted the first study to use scaled tsunami length waves to investigate scour at an onshore structure. They present the time development of scour around a square structure as a function of 147 s crest-led, 49 s trough-led and 25 s crest-led waves. Equilibrium was not attained, the rate of scour was time dependent, and published current and wave scour predictor equations over predicted the scour depth. Additionally, and crucially, the maximum scour depth was not equal to the end scour depth, suggesting that field investigations may underestimate the maximum scour depth, leading the ASCE 7-16 equation to under predict maximum scour depth.

This paper presents selected results from the same large-scale experimental campaign described in McGovern et al., (2019) on scour around coastal structures due to the inundation of tsunami waves. The paper focuses on the comparison of the scour time-development and structural loading experienced by two idealised geometric shape structures due to very long wave inundation.

2 Methods

A tsunami length crest-led wave of 147 s is generated by a unique Pneumatic Long Wave Generator (PLWG - as described in Rossetto et al., 2011 and McGovern et al., 2018). The PLWG, which is a steel box 4 m high, 3 m wide and 4 m long, is placed at the far end of the 75 m long, 4 m wide and 2.5 m deep Fast Flow Facility flume at HR Wallingford, U.K. As the set-up used in this paper is identical to that described in detail in McGovern et al., (2019), a concise description is provided here. Generated waves propagate along 23.9 m of constant depth followed by 20 m of 1:20 sloping bathymetry before impinging and inundating on a 3 m long horizontal sediment pit, divided into three parallel bays. In the outer bays, a symmetrical 0.2 m wide square Perspex cylinder is placed normal to the incident flow with the leading face 1 m downstream from the leading edge of the sediment pit (Fig. 1 and 2). In the central bay, a 0.4 m wide by 0.2 m deep rectangular Perspex cylinder is placed with the 0.4 m face normal to the incident flow. A fine, narrow graded sand ($d_{50} = 160$ microns) of depth 0.8 m is used in the pit and levelled flat before each test. A rectilinear coordinate system is used with $X = 0$ m being the start of the onshore region (the edge of the sediment pit), Z being the vertical coordinate (0 m at the sand surface, negative downwards) and Y being the lateral coordinate (set to 0 m at the centreline of each structure, and negative towards the right, Fig. 2).

Fig. 1.   A Cross-sectional schematic of the flume showing [1], the onshore region, [2] the nearshore region with 1:20 sloping bathymetry and [3] the offshore region of constant depth.
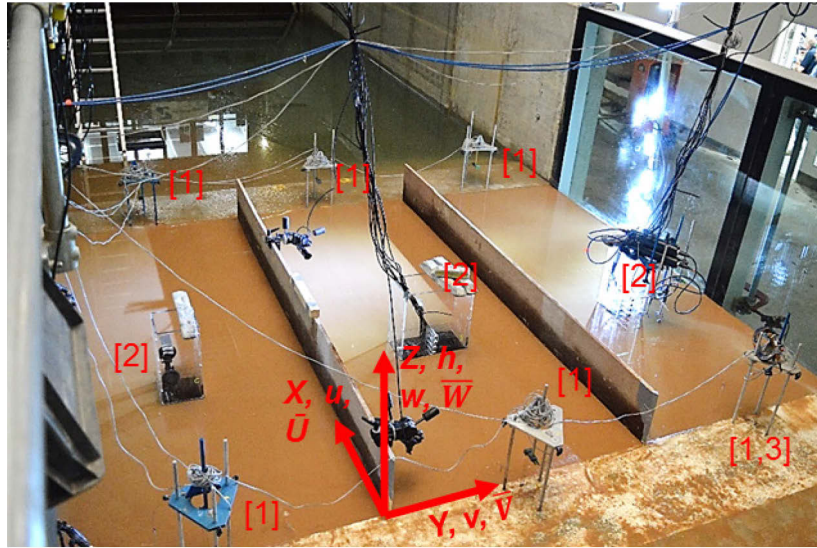
Fig. 2. Image of the flume sediment pit showing the 0.2 m square structures in the outer bays, and the 0.4 m rectangular structure in the centre bay [2]. [1] Depicts the onshore wave gauges and [3] the Vectrino II profiler.

Time-dependent free-surface elevation along the flume $\eta(X,t)$, where t is time, is recorded using resistance-type wave gauges manufactured by HR Wallingford. U is measured using a Vectrino profiler at $X = -1.1$ m in the right-hand bay (Fig. 2) as described in McGovern et al., (2019). As the Vectrino II requires full submersion of the probe head to give readings, the initial inundation is not reqorded (as depicted on Fig. 7 where there is a delay in the velocity record compared to the wave gauge record). As the inundation is not led by a bore front, the effect of aeration in the water column on the Vectrino II is minimal. Scour depth is measured using front-facing GoPro cameras inside each structure. The structures in the centre and right-hand bay (as viewed from Fig. 2) are fitted with pressure transducers vertically spaced along the centreline of the front face to record the wave pressure.

This paper focuses on these two structures only and the scour and loading from one wave run of the crest-led 147 s wave. Fig. 3 shows $\eta(X,t)$, as a function of normalised time t/T, in the offshore and nearshore regions for the wave. $T = t_{end} - t_{start}$ where t_{start} and t_{end} are defined as the times when $\eta(X,t)$ first up-cross and down-cross the value corresponding to 1% of a$^+$ (see also McGovern et al., 2018). T of the wave recorded at $X = -22.54$ m is used in the normalisation. This is the wave gauge in the offshore region that is nearest to the bathymetry toe, representing the position at which the waveforms are calibrated. This position is chosen as it represents a location where reflections off the slope are manifest almost instantaneously on the waveform and constitutes a definitive change in slope that is easier to define in a prototype. The definition point is discussed in detail in McGovern et al., (2018). It can be observed that the waveform is unchanged during propagation to nearshore.

3 Results

3.1 Tsunami Onshore Sediment Transport

A defined baseline of onshore tsunami scour for a known period, flow velocity and depth is not available in the literature. To establish a baseline, measurements of the overland flow and scour are made over an open, flat bed (Fig. 4a-b). Rippling is observed at the end of the test (Fig. 4b). The longitudinal spacing between ripples is $\approx$ 0.15 m and the amount of material lost from each bay is $\approx$ 0.012 m^3 (estimated from the amount of sand required to re-level the bay post-test). The mean transport rate q over the full inundation period is calculated to be 8.2 x 10^{-5} m^3/s, leading to a lowering of the average bed level by 3 mm. Observations during the tests show the transport regimes to be a combination of bedload and suspended load.
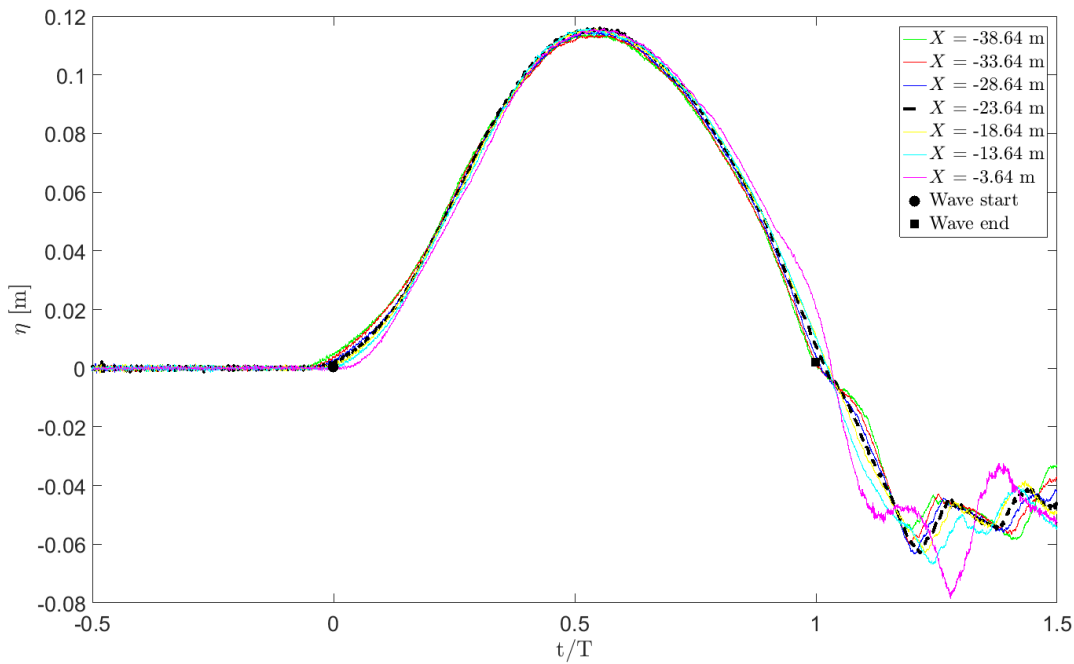
Fig. 3.   *η(X)* as a function of *t/T*.

Fig. 4.   A comparison of the sediment pit a) pre and b), post baseline test.

4 Tsunami Scour at Onshore Structures

The wave run where the structures are in place are now considered. Fig. 5a-j shows GoPro video images of the scour development at selected intervals of *t/T* at the front face of the square and rectangular structures (left and right columns respectively). The scour development at the square structure is discussed in detail in McGovern et al., (2019). Here, it is compared with the development observed around the rectangular structure.

For both structures, the scour initiates at the corners, and gradually moves towards the centerline. Both structures exhibit corner scour depths that far exceed those at the centerline, where the initiation of scour is delayed. The square structure scour hole forms, and retains, a triangular shape with apex at the centerline. The rectangular structure, however, exhibits a scour hole shape that is trapezoidal for the majority of the inundation with the region of no recorded scour extending laterally beyond the centerline. The triangular / trapezoidal shapes of the scour holes at both structures indicate that equilibrium is not achieved during a single inundation. Additionally, it is clear that the horseshoe vortex, usually the driving scour phenomena for monopile structures (Whitehouse, 1998), does not play a significant role in the scouring process at either structure. Rather, as described by McGovern et al., (2019) for the square structure, the scouring process is driven by the generation of a lateral base

vortex at the leading corner of the structure. This removes sediment from the corner, deepening the scour depth and removing any sediment that may slump inwards towards the corner. Over time, the sediment slumps towards the corners from across the front face, increasing the scour depth away from the corners. The reason for lack of scour at the centreline of the 0.4 m structure is presumably due to its greater width preventing this process from reaching the centreline over the same inundation period. This also implies that centreline scour would occur for longer inundation periods.

A key observation from McGovern et al., (2019) is the slumping of sediment towards the end of the inundation period due to the decrease in velocity of the flow. $d_{sc,max} = 0.104$ m on the front face of the square structure is observed at $t/T = 0.68$, after which significant slumping is observed. The end scour depth of $d_{sc,end} = 0.075$ m occurs at $t/T = 1.4$ and is approximately a third less than $d_{sc,max}$. The majority of slumping occurs between $t/T = 0.68 - 0.82$ as the inundation slows and velocities approach zero (see McGovern et al., 2019). For the rectangular structure, $d_{sc,max} = 0.14$ m occurs at $t/T = 0.67$. Slumping then reduces the scour depth to $d_{sc,end} = 0.1$ m at $t/T = 1.16$. The majority of slumping occurs between $t/T = 0.68 - 1.16$.

In the case of circular cylinders, scour depth increases as H/D increases up to a limiting value (for example, Ettema, 1980 and Chiew, 1984), therefore a larger $d_{sc,max}$ for the 0.2 m wide structure may be expected considering the flow depth (H) to structure diameter D ratio H/D (0.47) is larger than it is for the 0.4 m wide structure ($H/D = 0.23$). In shallower flows, the surface roller may interact with the downflow and horseshoe vortex, weakening one or both. As discussed, the horseshoe vortex does not appear to play a significant scouring role relative to the lateral vortex. It may, therefore be conjectured that the lateral vortex at the 0.4 m wide structure is stronger than at the 0.2 m wide structure. This may be due to the larger blockage provided by the 0.4 m structure, retarding the upstream flow to a greater extent and causing a greater acceleration around the sides of the structure due to the conservation of momentum. Thus, the boundary layer along the front leading face contains more momentum at the point of separation, leading to a stronger lateral vortex. The effects of the retardation of the upstream flow can be observed in the rippling of the bed upstream of the 0.2 and 0.4 m wide structures at the end of the test. The slowing of the flow upstream of the 0.4 m wide structure results in a smoother bed and fewer ripples (Fig. 6a-b). For both structures, rippling is comparatively less than for the baseline in Fig. 4b. The lateral extent of the scour hole is also greater for the 0.4 m wide structure.
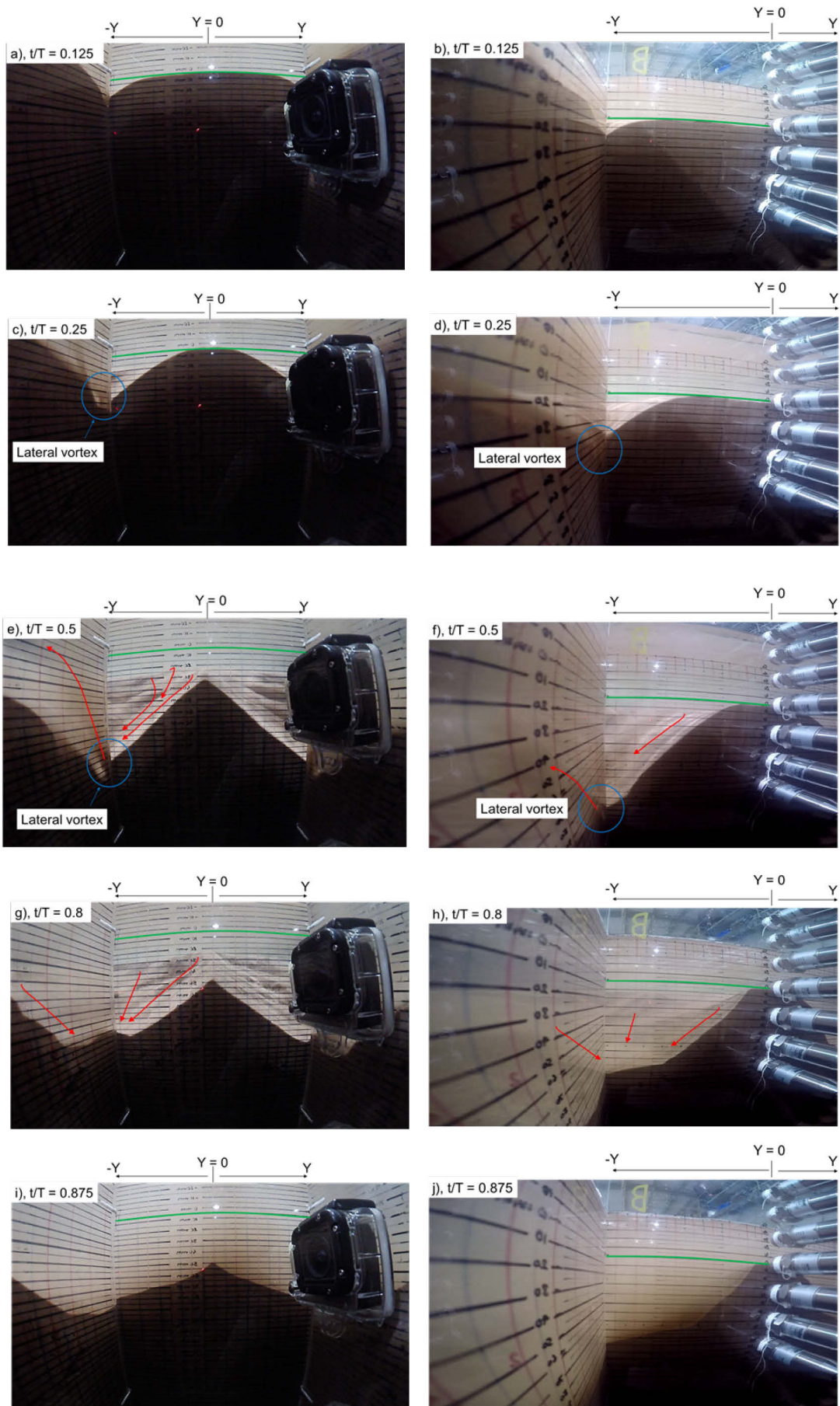
Fig. 5a-j. Front facing GoPro video stills from inside the square (left column, as reported in McGovern et al., 2019) and rectangular (right column) structures at variable intervals of t/T capturing the significant processes during the scour development. The green line denotes the original bed level where $Z = 0$ m. The wave propagation direction is out of the page, with the cameras filming from behind the front face of each structure. Refer to text for detailed explanation of annotations.
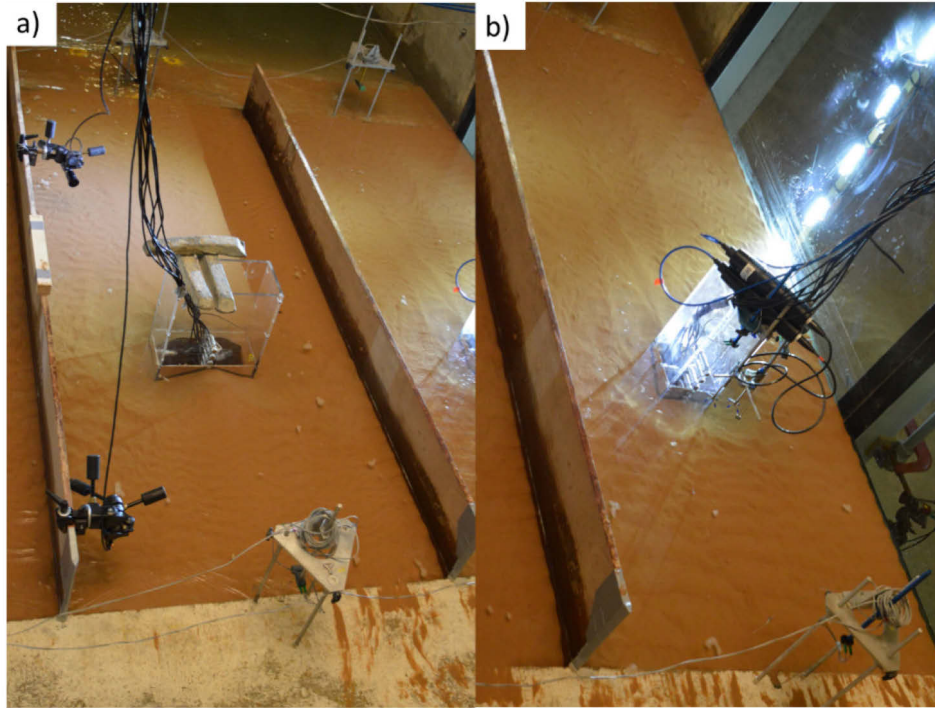
Fig. 6.   a) Image of the 0.4 m structure and b), the 0.2 m structure at the end of the test. Note the wider scour hole in a), along with smaller ripples in the immediate upstream region.

5 Tsunami Forces at Onshore Structures

For long period non-breaking tsunami, in which the Froude number Fr < 1, (where Fr = $U/\sqrt{(gH)}$), the load on the structure is a combination of the hydrostatic and hydrodynamic drag forces (e.g., Foster et al., 2017). The hydrostatic force $F_{h,stat}$ (Eq. 1) at the structure is estimated from the integration of the pressure readings along the front face, while the hydrodynamic drag force F_{dyn} is estimated using Eq. 2. Both equations are recommended in the ASCE (2016) design standard. Additionally, Foster et al., (2017) show that the integration of pressure readings provides a very good prediction for tsunami loading on onshore structures.

$$F_{h,stat} = \rho g h b \int_0^h h - z \, dz \qquad (1)$$

where ρ = fluid density, g = gravity, h = the height of the structure, b = the width of the structure and z = height of each pressure transducer. In the absence of impulsive wave pressures and integrating, Eq. 1 becomes

$$F_{h,stat} = \frac{1}{2}\rho g h^2 b \qquad (2)$$

The hydrodynamic drag may be computed from

$$F_{dyn} = \frac{1}{2}\rho C_d A U^2 \qquad (3)$$

where $A = hb$, C_d is the drag coefficient, and U is the flow velocity.

    The hydrostatic force at the structure should be calculated as the resultant force $F_{h,rslt}$, taking the water level at the rear of the structure into account through Eq. 4.

$$F_{h,rslt} = \frac{1}{2}\rho g b [H^2 - H_b{}^2] \qquad (4)$$

where H_b is the water depth directly behind the structure. Generally, $H_b < H$. A similar method is used in experiments by Shafiei et al., (2016) to compute conduct $F_{h,rslt}$ due to tsunami bore impact on square structures.

To evaluate Eq. 3, linear momentum flux per unit mass and width $H\overline{U}^2$ over time is computed, (where $\overline{U}$ is the depth-averaged velocity computed from the Vectrino II profiler at $X = -1.1$ m. $H\overline{U}^2$ is proportional to the drag force per unit width of a surface-piercing structure and can be used to estimate the net drag force on the structure (Yeh, 2006). Drag coefficient may be estimated by assuming a quasi-steady flow as $C_d \approx 2$ for a square structure (Yeh, 2006 and FEMA 2008). Fig. 7a shows $H(t)$ and $\overline{U}$, and 7b $H\overline{U}^2$ at $X = -1.1$ m. It is noted that this location is not at the equivalent position of the structure, as suggested by FEMA (2008), and that $\overline{U}$ is taken over the bottom 3.5 cm of flow depth only. With these caveats, $H\overline{U}^2$ is evaluated to estimate F_{dyn}. Maximum $H\overline{U}^2$ occurs $t/T = 0.285$ after the wave front reaches $X = 0$ m at $\approx 2/3$ H_{max} on the rise of the crest (Fig. 7a).
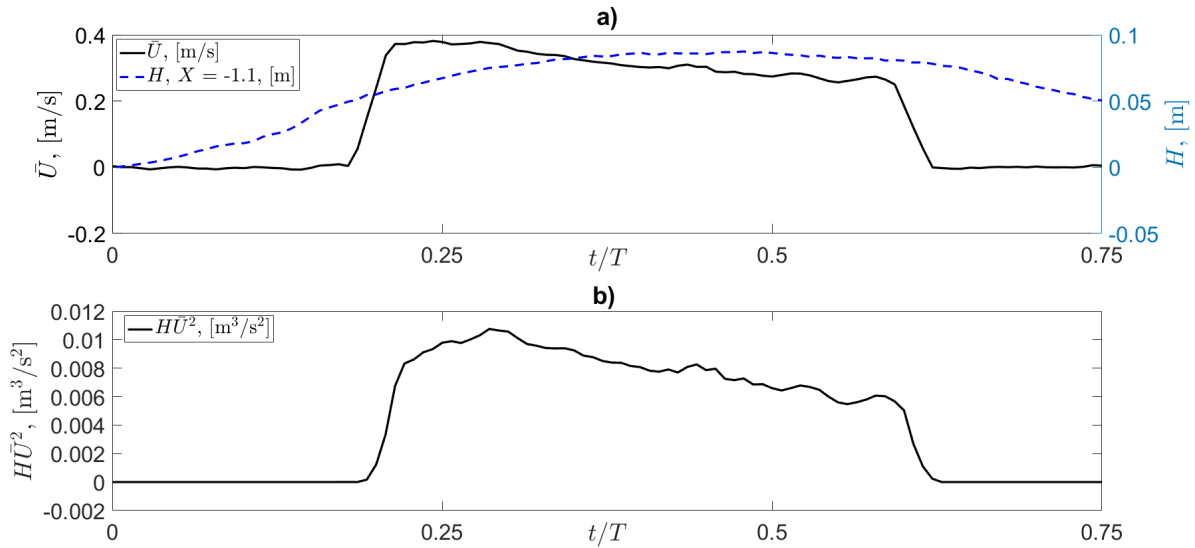

Fig. 7. a), $\overline{U}$, H and b), $H\overline{U}^2$ as a function of t/T, for wave run 1.

Figs 8a-b shows F_{dyn} (Eq. 3), F_h (Eq. 1 + d_{sc} at $Y/D = 0$) and F_{theory} (where H is derived from the first pressure transducer above the sand level at $Z = 0.035$ m + d_{sc} at $Y/D = 0$), as calculated from the integration of the pressure readings added to d_{sc} at $Y/D = 0$), as a function of t/T. Fig. 8b shows the corresponding values as calculated from the integration of the pressure readings added to d_{sc} at $Y/D = -0.425$. This is to demonstrate the large variation on recorded F_h that occurs depending on which $d_{sc}(t)$ value is used along the front face of the structure. The value of $H(t)$ used to calculate $F_{h,theory}$ is taken from the pressure transducer reading at $Z = 0.035$ m over the transducer at $Z = 0$ to avoid interference from the sand bed at this height, however, use of this transducer introduces a short delay in the first $F_{h,theory}$ value compared to F_h. Additionally, on both Fig. 8a and 8b, $F_{h,theory}^{\dagger}$ and $F_{h,theory}^{\ddagger}$ respectively show theoretical hydrostatic force due to the inundation height above $Z = 0$, and due to scour depth d_{sc} below $Z = 0$ (extracted from $Y/D = 0$ in a) and -0.425 in b)). This allows analysis of the contribution to the overall hydrostatic load between the inundation above the original bed level and scour hole.

Maximum F_{dyn} of 3 N occurs at $t/T = 0.285$, after the wave impact, with maximum F_h occurring in line with H_{max} at $t/T = 0.464$ (Fig. 7a). $F_h = F_{h,theory}$ throughout the wave, indicating that impulsive pressures are not present, as may be expected for non-breaking tsunami waves. Maximum total force at any time during inundation occurs when F_h is maximum (≈ 14 N) indicating that the hydrostatic load dominates the overall tsunami load. $F_{h,rslt}$, as defined in Eq. 4, is calculated by extracting H_b from the side-facing pressure transducer located at $X = 0$, $Y/D = 0.5$ (see Fig. 8d, which shows the centreline sediment depth to be relatively unchanged except near the corners. Therefore, in light of a lack of direct measurement of H_b, the side-facing pressure measurement is used to give a reasonable estimation of $H-H_b$. The maximum $F_{h,rslt}$ is 7.35 N and 14.81 N at $t/T = 0.51$ and $t/T = 0.6$, when $F_{h,theory}^{\dagger}$ and $F_{h,theory}^{\ddagger}$ are accounted for, respectively.

For the rectangular structure, there is no scour along the centerline ($F_{h,theory}^{\dagger} = 0$ N), hence the hydrostatic force is due to H alone. The drag force is likely to be greater, due to the larger velocities generated by the greater flow constriction past the sides, though this is not directly measured. Maximum values of H and H_b are estimated from the GoPro video giving 0.115 m and 0.065 m respectively. This leads to $F_{h,rslt} = 17.7$ N at the centreline. At $Y/D = -0.475$ (the location of the scour depth reading closest to the structures corner), $d_{sc,max} = 0.14$ m leads to a maximum $F_h = 128$ N and a $F_{h,rslt} = 119$ N. Clearly the resultant forces are greater because of the greater blockage ratio of the 0.4 m structure in comparison to the 0.2 m structure. This results in lower values of H_b due to the greater drop in the free surface between the front and rear of the structure. This is in addition to the significantly greater depth of scour achieved due to the larger velocities generated.

To accurately estimate the resultant force on either structure as a function of time will require the integration of the force both vertically and horizontally around the surface of the structure. The resultant force is likely less than this when the side and rear scour values are considered, and this will be evaluated in an upcoming publication.
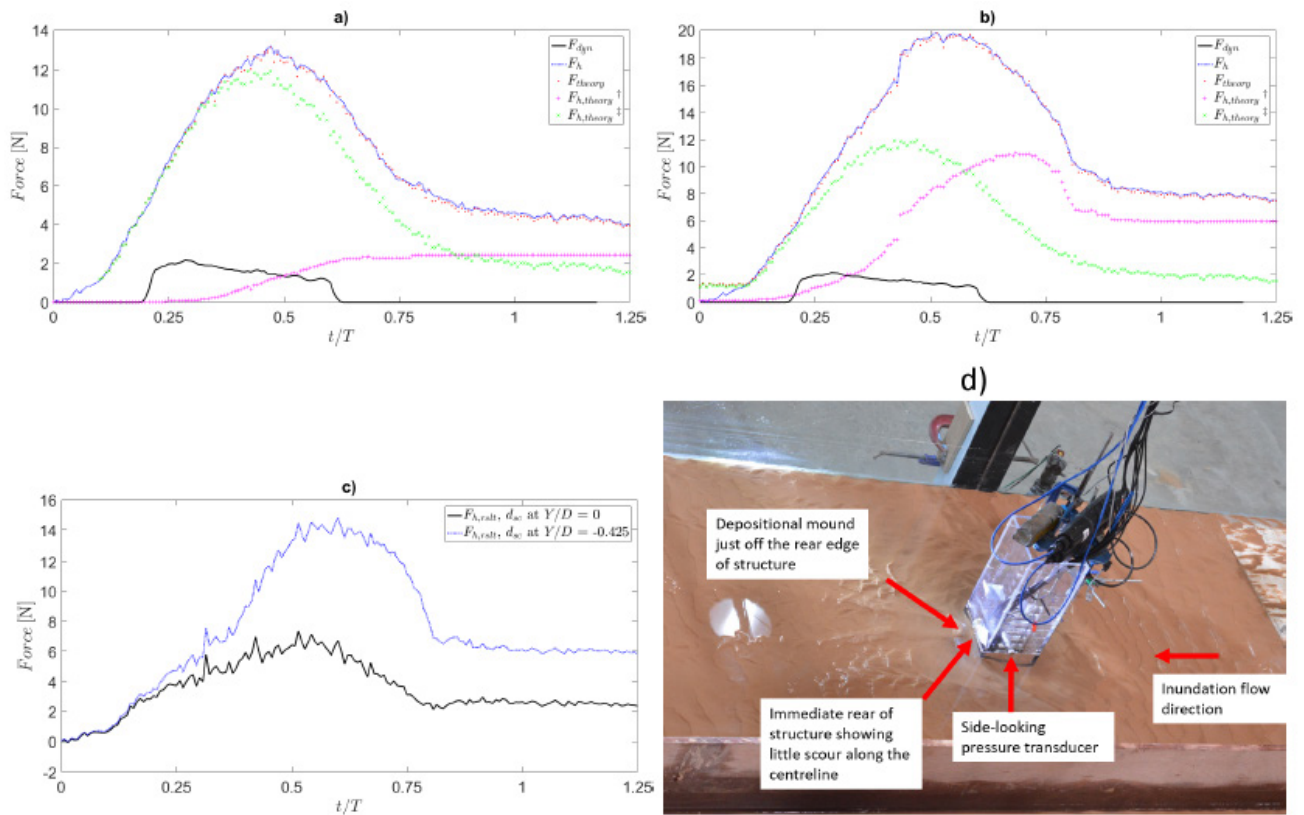

Fig.8.   a-b show F_{dyn} F_h, $F_{h,theory}$ and $F_{h,theory}^{\dagger}$ and $F_{h,theory}^{\ddagger}$ in which where relevant, d_{sc} is extracted at $Y/D = 0$ and $Y/D = -0.425$, respectively. c), $F_{h,rslt}$ when the d_{sc} value at $Y/D = 0$ (black -) and -0.425 (blue -) is used as a function of t/T. d), post-scour image showing little change in sediment level at the rear of the 0.2 m square structure.

6 Conclusions

This paper presents results from a large-scale series of long wave scour experiments at onshore structures. The wave period of 147 s is scalable to tsunami at prototype. Scour around two structures, a 0.2 m by 0.2 m square and a 0.4 m wide by 0.2 m deep rectangle is recorded using internally mounted GoPro cameras. Scour is observed to develop in a similar manner for both structures, starting at the leading corner and moving towards the centerline during the inundation. The observed scour processes are different to those typically observed for monopiles, being mainly driven by a lateral vortex, rather than by downflow and horseshoe vortex. Maximum scour depth occurs during inundation, before slumping reduces the depth, resulting in lower end scour depths. Both maximum and end scour depth for the 0.4 m rectangular structure are 29% greater than for the 0.2 m square

structure, apparently due to the weaker lateral vortex for the latter. For both structures, the hydrostatic load was greater than the hydrodynamic load. The loading varies as a function of position with the scour depth variation along the front face of the structure; larger hydrostatic loads are experienced at the sides of the structure due to the large scour depth at those locations. Maximum resultant force was 119 N for the rectangular structure, which is much greater than for the square structure (14 N).

The data reported is part of a large experimental campaign; a future publication will build on this and address the influence of structure shape, angle of attack, sheltering on scour and loading for a variety of wave periods and shapes.

Acknowledgements

References

ASCE 2016. ASCE/SEI 7-16 Chapter 6: Tsunami Loads and Effects.

Chiew, Y. M., (1984) Local Scour at Bridge Piers. Auckland, Auckland University.

Chock, G., Robertson, S. E., Kriebel, D., Francis, M., and Nistor, I. 2013. Tohoku, Japan, Earthquake and Tsunami of 2011. ASCE.

EEFIT 2004. The Indian Ocean tsunami of 26 December 2004 mission findings in Sri Lanka and Thailand. Technical report, Institution of Structural Engineers.

EEFIT 2011. The mw 9.0 Tohoku Earthquake and Tsunami of 11th March 2011. Technical report, Institution of Structural Engineers.

Ettema, R., (1980) Scour at Bridge Piers. University of Auckland.

FEMA 2008, FEMA P646, guidelines for design of structures for vertical evacuation from tsunamis, FEMA.

Foster, A. S. J., Rossetto, T., and Allsop, W. 2017. An experimentally validated approach for evaluating tsunami inundation forces on rectangular buildings. Coastal Engineering, 128, 44-57.

Kajitani, Y., Chang, S. E., and Tatano, H. (2013). Economic impacts of the 2011 Tohoku-Oki Earthquake and Tsunami. Earthquake Spectra, 29 (S1) S457-S478.

Madsen, P., Fuhrman, D., and Schäffer, H. 2008. On the solitary wave paradigm for tsunamis. Journal of Geophysical Research, 113 (C12012).

McGovern, D. J., Robinson, T., Chandler, I. D., Allsop, W., and Rossetto, T. 2018. Pneumatic long-wave generation of tsunami-length waveforms and their runup. Coastal Engineering, 138, 80-97.

McGovern, D.J., Todd, D. Rossetto, T., Whitehouse, R.J.S., Monaghan, J. and Gomes, E., 2019. Experimental Observations of Tsunami Scour at Coastal Structures. Coastal Engineering, In Press, https://doi.org/10.1016/j.coastaleng.2019.103505

Mori, N. and Takahashi, T. 2012. The 2011 Tohoku Earthquake and Tsunami joint survey group. Nationwide post event survey and analysis of the 2011 Tohoku Earthquake and Tsunami. Coastal Engineering Journal, 54 1-27.

Nakamura, T., Kuramitsu, Y., and Mizutani, N. 2008. Tsunami scour around a square structure. Coastal Engineering Journal, 50 (2), 209-246.

Rossetto, T., Allsop,W., Charvet, I., and Robinson, D. 2011. Physical modelling of tsunami using a new pneumatic wave generator. Journal of Coastal Engineering, 58, 517-527.

Shafiei, S., Melville, B. W. and Shamseldin, A. Y. 2016, Experimental investigation of tsunami bore impact force and pressure on a square prism, Coastal Engineering, 110, 1-16.

Telford, J., Cosgrave, J., and Houghton, R. 2006. Synthesis report: Joint evaluation of the international response to the Indian Ocean tsunami. Technical report, Tsunami Evaluation Coalition (TEC).

Tonkin, S. P., Francis, M., and Bricker, J. D. 2013. Limits on coastal scour depths due to tsunami. In Davis, C., Du, X., Miyajima, M., and Yan, L., editors, International Efforts in Lifeline Earthquake Engineering, volume TCLEE 38.

Tonkin, S., Yeh, H., Kato, F., and Sato, S. 2003. Tsunami scour around a cylinder. Journal of Fluid Mechanics, 496, 165-192.

Whitehouse, R. J. S. 1998. Scour at Marine Structures. Thomas Telford.

Yeh, H., Franci, M., Peterson, C., Katada, T., Latha, G., Chadha, R. K., Singh, J. P., and Raghuraman, G. 2007. Effects of the 2004 Great Sumatra Tsunami: Southeast Indian Coast. Journal of Waterway, Port, Coastal and Ocean Engineering, 133(6), 382-400.

Yeh, H. 2006, Maximum fluid forces in the runup zone, Journal of Waterway, Port, Coastal and Ocean Engineering, 132 (6), 496-500.